
FORMATION OF MASSIVE, DENSE CORES BY CLOUD-CLOUD COLLISIONS

Ken TAKAHIRA¹, Kazuhiro SHIMA,^{1*}, Elizabeth J. TASKER^{2*}, and Asao HABA^{1*}

¹Graduate School of Science, Hokkaido University, Kita 10 Nishi 8, Kita-ku, Sapporo 060-0810, Japan

²Institute of Space and Astronautical Science (ISAS), Japan Aerospace Exploration Agency (JAXA), Sagami-hara, Kanagawa 252-5210, Japan

*E-mail: shima@astro1.sci.hokudai.ac.jp, elizabeth.tasker@jaxa.jp, habe@astro1.sci.hokudai.ac.jp

Received ; Accepted

Abstract

We performed sub-parsec (~ 0.014 pc) scale simulations of cloud-cloud collisions of two idealized turbulent molecular clouds (MCs) with different masses in the range of $0.76 - 2.67 \times 10^4 M_{\odot}$ and with collision speeds of $5 - 30$ km/s. Those parameters are larger than Takahira, Tasker and Habe (2014) (paper I) in which the colliding system showed a partial gaseous arc morphology that supports the NANTEN observations of objects indicated to be colliding MCs by numerical simulations. Gas clumps with density greater than 10^{-20} g cm⁻³ were identified as pre-stellar cores and tracked through the simulation to investigate the effect of mass of colliding clouds and collision speeds on the resulting core population. Our results demonstrate that smaller cloud property is more important for results of cloud cloud collisions. The mass function of formed cores can be approximated by a power law relation with index $\gamma = -1.6$ in slower cloud cloud collisions ($v \sim 5$ km/s), in good agreement with observation of MCs. A faster relative velocity increases the number of cores formed in the early stage of collisions and shortens gas accretion phase of cores in the shocked region, leading to suppression of core growth. The bending point appears in the high mass part of the core mass function and the bending point mass decreases with increasing of the collision velocity for the same combination of colliding clouds. The high mass part of the core mass function than the bending point mass can be approximated by a power law with $\gamma = -2.3$ that is very similar to the power index of the massive part of the observed initial stellar mass function. We discuss implication of our results for the massive star formation in our Galaxy.

Key words: ISM: clouds — Stars: formation — Methods: numerical — Hydrodynamics

1 INTRODUCTION

Massive star formation is very important in astrophysics, since massive stars play important roles in galaxy formation and evolution. However, the processes of massive star formation are not well understood. Recent observations show possible connection between massive star formation and cloud cloud collisions (Furukawa et al. 2009; Ohama et al. 2010; Torii et al.

2011; Fukui et al. 2014; Torii et al. 2015). Molecular lines observations of the two Super Star Clusters, Westerland 2 and NGC 3603 (Furukawa et al. 2009; Ohama et al. 2010; Fukui et al. 2014) and the Trifid Nebula (Torii et al. 2011) show two molecular clouds of relative velocities of $10 - 20$ km/s associated with these objects. Notably, the relative velocities observed in these three events are too high for the clouds to be gravita-

tionally bound to one another. Bridge features that appear in the position velocity diagrams in these observations are clear evidence of interaction by cloud cloud collisions (Haworth et al. 2015). The resulting shock waves between the clouds compress the gas and form dense gas that is possible to form the massive stars.

Torii et al. (2015) report two molecular clouds with relative velocities in the Spitzer bubble, RCW 120, as a evidence of cloud cloud collision. They also noted that the ring structure seen in RCW 120 is very similar to the product of cloud collisions by theoretical calculations by Habe & Ohta (1992), Anathpindika (2010), and Takahira, Tasker & Habe (2014) (paper I). Similar arc like structures are observed in galactic central molecular clouds (Higuchi et al. 2014; Tsuboi et al. 2015).

Habe & Ohta (1992) performed two dimensional, axisymmetric simulations of a head-on collision between non-identical smoothed clouds. They found that the larger cloud was disrupted by the resulting bow-shock which in turn, compressed the smaller cloud. This compression caused the post-shock gas in the smaller cloud to become gravitationally unstable, even in the case where the cloud was initially below its Jeans mass. The geometric structure of the collision shows the same ring-like morphology as seen in RCW 120, with dense cores for the expected star formation forming in the compressed shock, not in the center of the ring.

Studies of cloud collision frequency by performing numerical simulation of a Milky Way-type disk show that multiple collisions can occur per orbital period (Tasker & Tan 2009; Tasker 2011). Recent numerical studies report similar collision frequency (Fujimoto, Tasker, Wakayama & Habe 2014; Dobbs, Pringle & Duarte-Cabral 2015). This rate agrees with analytical estimation made by Tan (2000) who studied the rate of cloud collision that can explain the star formation rate in the galaxy, producing the empirical Kennicutt-Schmidt relation between gas surface density and star formation rate (Kennicutt 1998).

Since the observational studies and theoretical studies of cloud collision frequency support an idea of an important role of cloud cloud collisions in massive star formation, theoretical studies on possible connection between cloud cloud collisions and massive star formation are very interesting.

In paper I, we have studied cloud cloud collisions of rather less massive clouds ($417 M_{\odot}$ and $1635 M_{\odot}$) by numerical simulations, assuming hydrodynamic, turbulent internal motions in the colliding clouds before their collisions. We have shown that many clumps are formed by shock compression induced by cloud cloud collision, and a dense and massive clump as high as $100 M_{\odot}$ is finally formed with collision speeds 3 km/s and 5 km/s. Mass growth of dense clumps is mainly mass accretion of surrounding gas on the clump. In higher collision speed case, 10 km/s, clouds are highly compressed by shock wave induced

by the cloud cloud collision, but the duration time of collision is not long enough for growing of the clump mass by gas accretion and no dense and massive clump is formed. The numerical results of paper I indicate that we should simulate more large and massive clouds collision case for more higher collision speeds.

In this paper, we study cloud cloud collision of more massive clouds with larger collision speeds than paper I to examine formation of dense, massive clumps and to investigate the impact of collision speed on properties and evolution of these clumps. We assume initial clouds are $\sim 0.76 - 2.67 \times 10^4 M_{\odot}$. For more massive clouds than the mass range, cloud shape should be far from spherical. Since such massive clouds are formed in gas disk simulations in a galaxy scale (Benincasa et al. 2013; Fujimoto, Tasker, Wakayama & Habe 2014), we will study such massive clouds collisions by numerical simulations, by picking up them from results of a galaxy scale simulation in forthcoming paper. In order to resolve internal turbulence motion inside of dense clumps formed by cloud cloud collision, we improve our numerical resolution from 0.06 pc in paper I to 0.014 pc in this paper. We concentrate on study of mass function of dense gas clumps formed by cloud cloud collisions, since core mass function is very important for study of the stellar initial mass function (e.g. Tan et al. 2014). In §2 we describe the details of our simulation, in §3 we show our numerical results and we give discussions in §4 and summary in §5.

2 NUMERICAL METHODS

We use the same simulation method in paper I. Since the detailed information of the simulation method is described in paper I, we briefly summarize the simulation method. We used Enzo; a three-dimensional hydrodynamical adaptive mesh refinement code (Bryan et al. 2014; Bryan 1999; Bryan & Norman 1997). A boxsize of $120 \text{ pc} \times 120 \text{ pc} \times 120 \text{ pc}$, a root grid size of $128 \times 128 \times 128$ and an additional six levels of refinement were used, giving a limiting resolution (smallest cell size) of $\sim 0.014 \text{ pc}$. We used the refinement criteria based on gas mass and on the resolution of the Jeans length, which must be refined by at least four cells as suggested by Truelove et al. (1997). By using the resolution in our simulations, $\sim 0.014 \text{ pc}$, we can resolve turbulent cores which size is larger than $\sim 0.21 \text{ pc}$ (Federrath et al. 2010).

The hydrodynamics were evolved over time using a three-dimensional implementation of the Zeus astrophysical code (Stone & Norman 1992). To handle shocks, Zeus uses an artificial viscosity where the associated variable, the quadratic artificial viscosity term, set to 2.0 (the default value).

In order to prevent gas undergoing unrefined collapse on the finest grid level, we impose a pressure floor. In a collapsing region where the Jeans length can no longer be refined by the desired four cells, the pressure is increased so that the gas fol-

lows a polytrope with an adiabatic index $\gamma = 2.0$. This polytrope is stable and stops the collapse.

Gas cools radiatively down to 10 K using a one-dimensional cooling table created using the CLOUDY cooling code (Ferland et al. 1998) where solar metallicity and a density of 100 cm^{-3} was assumed. For the densities achieved in our simulation, the cooling function remains relatively constant, allowing us to use this simplification.

2.1 Core identification and tracking

Dense cores are identified in the simulation via a constant density contour finding algorithm (Turk et al. 2011). In the finding algorithm, we use four density thresholds that are $\rho_{crit} = 10^{-20} \text{ g cm}^{-3}$, $\rho_{crit} = 5 \times 10^{-20} \text{ g cm}^{-3}$, $\rho_{crit} = 10^{-19} \text{ g cm}^{-3}$ and $\rho_{crit} = 5 \times 10^{-19} \text{ g cm}^{-3}$ to study how dense cores evolve with time. We note that the average GMC density is observed to be $\sim 100 \text{ cm}^{-3}$ while star formation is seen to occur in dense cores of $\gtrsim 10^4 \text{ cm}^{-3} \sim 3 \times 10^{-20} \text{ g cm}^{-3}$ (Ginsburg et al. 2012; Lada, Lombaridi & Alves 2010). Therefore within these cores, gravity is likely to dominate over other physical processes to result in star formation. In order to analyze the evolution of the core properties, we track their motion over the time of the simulation. This process is performed in a similar manner to the cloud tracking scheme presented in Tasker & Tan (2009) and paper I.

2.2 The initial condition

Initial condition of clouds are similar to paper I, but for more massive masses and larger sizes for clouds. The simulation initial conditions consist of two clouds of unequal masses whose boundaries are separated by approximately 1.2 pc. The density distribution of each cloud is assumed to be the form of a Bonner-Ebert sphere (Bonner 1956); a hydrostatic isothermal self-gravitating gas sphere that is confined by its external pressure. The maximum mass such a sphere is given by:

$$M_{BE} = \frac{c_{BE} c_s^4}{P_{ext}^{\frac{1}{2}} G^{\frac{3}{2}}} = 4600 \left(\frac{c_s}{1 \text{ km/s}} \right)^4 \left(\frac{P_{ext}}{4000 k_B} \right)^{-\frac{1}{2}} M_{\odot}, \quad (1)$$

where c_s is the isothermal sound speed, $c_{BE} = 1.18$ is a constant, P_{ext} is the external gas pressure, k_B is the Boltzmann constant and G is the gravitational constant. A cloud with mass, M_C less than M_{BE} is dynamically stable. The simulated clouds fulfill this stability requirement. Their properties are summarized in Table 1. Once cooling begins, the cloud becomes unstable and without additional support, will start to collapse. The density profile was primarily chosen because the initial stability is appealing when considering the impact of outside effects. However, dense molecular clouds have also been observed to show a Bonner-Ebert density profile in the work of Alves et al.

Table 1. Initial cloud model parameters.

	Small	Medium	Large	Constant
M_C (M_{\odot})	7613	14935	26722	20398
r_c (pc)	14.4	20.9	28.0	10.0
\bar{n} (cm^{-3})	24.47	15.94	11.86	120.4
σ_v (km/s)	2.62	3.17	3.57	3.01
T_{BE} (K)	480	720	960	700
t_{ff} (Myr)	10.4	13.0	15.0	4.71
k-mode	5 – 12	10 – 19	10 – 25	8 – 16

(2001). Adding to the Bonner-Ebert profile clouds, we use the constant clouds that have a higher density and mass@ than the Bonner-Ebert mass. The clouds are not in free-fall collapse, due to additional support from internal turbulent motions. This allows c_s in the above equation to be switched for the effective sound speed that also including a contribution from the velocity dispersion. In Table 1, we show physical parameters of the initial clouds. T_{BE} is temperature of the clouds and σ_v is the velocity dispersion corresponding to T_{BE} . Initial clouds' radius and velocity dispersion are roughly consistent with the Larson relation (Larson 1981; Heyer et al. 2009).

2.3 Turbulence

In simulations, we impose a velocity field on initial clouds with power spectrum $v_k^2 \propto k^{-4}$, corresponding to the expected spectrum given by Larson (1981) for giant molecular clouds. To ensure the turbulence modes were adequately resolved, we selected a maximum k -mode value of 1/10 th of the number of cells across the cloud. In addition, we removed the lower order modes since these larger-scale perturbations disrupted the cloud structure, causing it to fragment prior to collision. Since the focus of this paper is on the impact of the cloud collision, we selected turbulence modes that would initially stabilize the isolated clouds, preventing collapse prior to collisional contact from the gas cooling. We summarize k range in Table 1. As shown in paper I, we confirmed that clouds are stabilized more than their free fall time by turbulent motions. The amplitude of the turbulence is specified by the Mach number, $M = \sigma_v/c_s$, where σ_v is the velocity dispersion inside the cloud and c_s is the sound speed. In the initial cloud, we assume that $M = 1$.

When turbulence is applied, the clouds remain in their static positions for 0.5 Myrs. This allows the clouds to reach a new state with the turbulent support, as measured by their volume density distribution that is called the probability density distribution function (PDF) evolving to the expected lognormal profile for super-sonic isothermal turbulent gas (Vazquez-Semadeni 1994; Ostriker et al. 1999).

PDF of the Small, Medium and Large clouds with the turbulent support are shown in Figure 1. The blue dashed line marks a log-normal profile with equation:

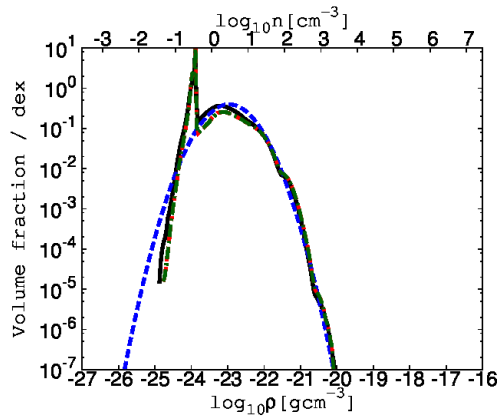


Fig. 1. Probability Distribution Functions (PDFs) for the Small, Medium and Large Clouds before collision, at 1.0 Myr. The blue dashed line shows a lognormal fit. The green chain line shows the gas of the Small Cloud, the red solid line is the Medium cloud and the black dotted line is the Large cloud. Before collision, these clouds gas above a density of $\sim 10.0 \text{ cm}^{-3}$ are well fitted with the log-normal form.

$$f(x; \mu, \sigma) = \frac{A}{\sigma\sqrt{2\pi}} e^{-\frac{1}{2}\left(\frac{x-\mu}{\sigma}\right)^2} \quad (2)$$

where $x = \ln \rho / \bar{\rho}$ and the constants have values $A \sim 1.2$, $\mu = 0.0$ and $\sigma = 1.2$. The green chain line shows the gas of the Small Cloud at 1.0 Myr, the red dotted line is of the Medium Cloud and the black solid line is of the Large Cloud. In all clouds, the gas above a density of $\sim 10.0 \text{ cm}^{-3}$ closely follow a lognormal distribution before collision, as shown in paper I. This result agrees strongly with the observations from Kainulainen et al. (2009), who find that giant molecular clouds without active star formation show a log-normal distribution.

The collisions between these clouds in Table @1 were performed under variety of (1) different collision speeds, (2) different combination of colliding cloud sizes, and (3) different cloud density profiles. In the first part, we show the results of the Medium and Large clouds collisions with velocities 5 km/s, 10 km/s 20 km/s and 30 km/s. In the second part, size combinations of clouds are Small-Medium, Small-Large, Medium-Medium and Medium-Large, with a collision velocity of 10 km/s. In the final simulations, we assume a constant density cloud for smaller cloud.

3 RESULT

3.1 The effect of collision speeds

The time evolutions of cloud cloud collisions between the same combination of clouds, Medium and Large clouds, with collision speeds, 5 km/s, 10 km/s 20 km/s and 30 km/s are compared. These speeds are in the range of cloud collision velocities found in global numerical simulation of cloud formation in a barred galaxy (Fujimoto, Tasker, Wakayama & Habe 2014).

The evolution of these four simulations is shown in Figure 2, with time progressing from left to right. Each image shows the surface density averaged over a depth of 2.0 pc. The top row of three panels shows the evolution of the simulation with a cloud collision speed of 5.0 km/s, the second row shows the results of 10 km/s, the third row shows the results of 20 km/s and the bottom row shows the results of 30 km/s. The times shown correspond to the same event in each simulation: the left-hand panels show the first touching (2.1, 1.9, 1.1 and 0.9 Myr, for the 5 km/s, 10 km/s, 20 km/s and 30 km/s simulation after the runs begin, respectively), the middle panels show the time when the number of cores attains its maximum (12.9, 7.4, 4.1 and 2.9 Myr). The final right-hand panels show the time when the core number is roughly steady (21.6, 12.8, 8.8 and 8.5 Myr, here after we call this epoch the converge point), where we shift each x -origin of the coordinate as, x (5 km/s), $x+20$ pc (10 km/s), $x+60$ pc (20 km/s) and $x+80$ pc (30 km/s), since the boundary condition of our simulation box is periodic.

In the middle panels, Medium Clouds are compressed by shock waves and the partial arcs of dense gas are formed. These arcs have irregular ripple structures due to the Rayleigh-Taylor instability and the thin shell shock instability. Since the initial size of the Medium cloud is 1.5 times smaller than the size of Large cloud, the arcs are widely open. As shown in subsection 3.2, when a size of smaller clouds is smaller, partial arcs formed by cloud cloud collisions become more close. At the converge points, in the right panels, the elongated filament structures are formed and, in higher collision speed, the filamentary structure appears more clearly and becomes oscillatory with larger amplitude.

3.1.1 Probability distribution function

The probability distribution functions (PDFs) are shown in Figure 3 for the four simulation results of the different collision velocities at the converge points. PDF is for gas within a sphere of 30 pc radius centered on Large Cloud. The blue dashed line in all panels is same as the log-normal profile in Figure 1. In Fig. 3, the top-left shows the result for the 5.0 km/s case and the top-right is for the 10 km/s case, while on the bottom row the left-hand panel shows the 20 km/s simulation and the right-hand panel shows the 30 km/s simulation. The converge points in each panel are , 21.6 Myr, 13.5 Myr, 9.0 Myr and 7.9 Myr for the collision velocities, 5, 10, 20 and 30 km/s, respectively. In all four collisions cases, PDF tails extend from the log-normal to the higher gas density. This extension is most marked in the 5 km/s and 10 km/s collisions and is present, but less extended, in the 20 km/s and 30 km/s run. The tail consists of a power law tail and a shallower extension at the higher density part. Power index of the power law tail is approximately -1.5 that well agrees with simulations of gravitational collapse of a turbulent cloud by Kritsuk et al. (2011).

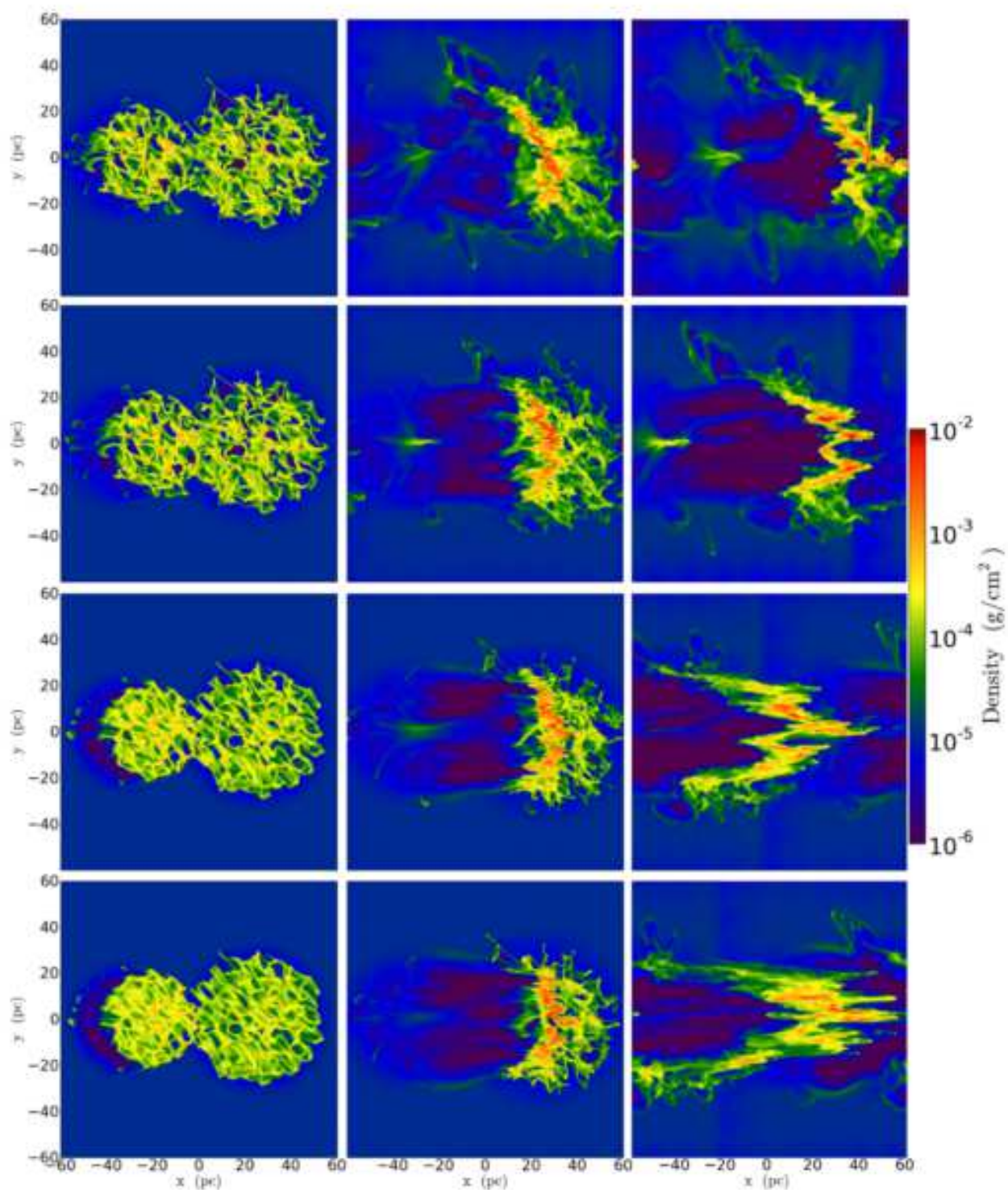


Fig. 2. Thin (2.0 pc thickness) projections showing the evolution of the surface density during the Medium Cloud and Large Cloud collision at the different relative velocities. The three times shown correspond to the initial contact between the two clouds (left), the maximum number of formed cores (middle) and the converging point (right) in each case. From top to bottom, the collisional velocities are 5.0 km/s, 10 km/s, 20 km/s and 30 km/s.

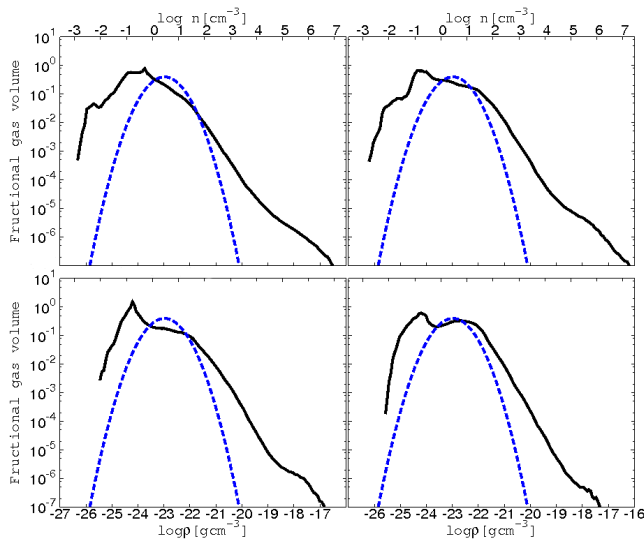


Fig. 3. The probability distribution functions (PDF) for the Medium and Large clouds collisions at the converge point with different relative velocities. The black solid line shows the profile for each run at the converge point while the blue dashed line shows the log-normal fit for turbulent clouds before the collision. The top-left plot shows the result in the 5 km/s collision case, the top-right is for the 10 km/s, the bottom-left is for the 20 km/s and the bottom-right is for the 30 km/s simulation. In all cases, the PDFs deviate from the log-normal profile to extended tails in the high density as cores form.

Kritsuk et al. (2011) have given the argument that can explain the index of the power law tail by the gravitationally collapsing isothermal gas structures. From their study, the power law tail is evidence of self-gravitational collapse of dense gas induced by cloud cloud collision. The result of the deviation from the log-normal form agrees with the observations by Kainulainen et al. (2009), who shows that giant molecular clouds displaying star formation show prominent non-log-normal wings, while giant molecular clouds without active star formation show the log-normal distribution.

3.1.2 Core number evolution

The time evolution of the core number plotted as a fraction of the free-fall time of Medium Cloud, $t_{ff1} = t_{ff,M}$, is shown in Figure 4 until the converging point. These panels show the core number evolution for the runs with the collisional speed, 5 km/s (top-left), 10 km/s (top-right), 20 km/s (bottom-left) and 30 km/s (bottom-right). The initial time in the plots, $t = 0$, corresponds to the time when the clouds surfaces touch. In each plot, we use four different density values for the core definition to show the fragmentation of the shocked gas formed by cloud cloud collisions: $\rho_{crit} = 10^{-20} \text{ g cm}^{-3}$ (black solid line), $\rho_{crit} = 5 \times 10^{-20} \text{ g cm}^{-3}$ (red dashed line), $\rho_{crit} = 10^{-19} \text{ g cm}^{-3}$ (gray dot line) and $\rho_{crit} = 5 \times 10^{-19} \text{ g cm}^{-3}$ (blue chain line). We restrict the cores plotted to those containing more than 27 cells to ensure the best resolution.

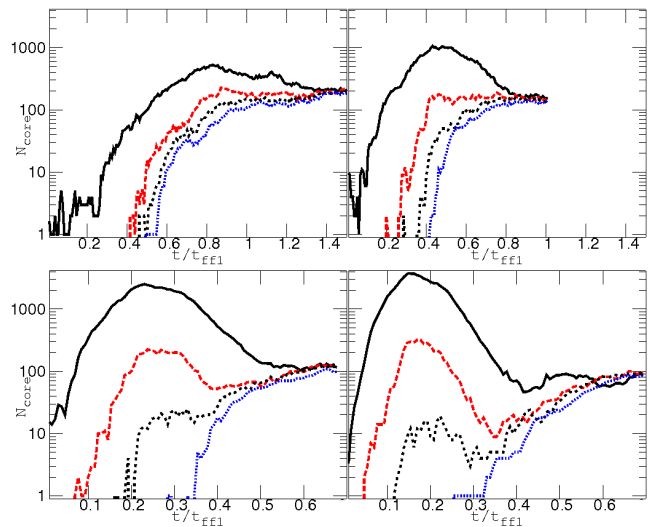


Fig. 4. Time evolution of core number as a fraction of Medium Cloud's free-fall time for collisions between Medium and Large Clouds for four different collision velocities. The panels show the collision for 5 km/s (the top-left), 10 km/s (the top-right), 20 km/s (the bottom-left) and 30 km/s (the bottom-right). $t/t_{ff1} = 0$ corresponds to the time just prior to collision when the cloud surface are touching. The lines in each panel show core numbers at different density thresholds, as the black solid line for $1 \times 10^{-20} \text{ g cm}^{-3}$, the red dashed lines for $5 \times 10^{-20} \text{ g cm}^{-3}$, the gray dotted lines for the threshold of $1 \times 10^{-19} \text{ g cm}^{-3}$ and the blue chain lines for $5 \times 10^{-19} \text{ g cm}^{-3}$.

As shown in Figure 4, the core number for $\rho_{crit} = 10^{-20} \text{ g cm}^{-3}$ (black solid line) increases to its maximum, after then, decreases with time and finally attains a steady state at the converging points. The time and values for the maximum number of cores depend on the collision velocity, with the higher relative speed creating more numerous cores rapidly. The peak epochs are $0.8 t_{ff,M}$ for 5 km/s, $0.45 t_{ff,M}$ for 10 km/s, $0.22 t_{ff,M}$ for 20 km/s and $0.16 t_{ff,M}$ for 30 km/s. The decrease of core number after the peaks means that density of $\rho_{crit} = 10^{-20} \text{ g cm}^{-3}$ is not enough to keep a core structure for the collision velocity of 5–30 km/s. Peaks of core number also appear in red lines ($\rho_{crit} = 5 \times 10^{-20} \text{ g cm}^{-3}$) for 20 km/s and 30 km/s and in the gray line ($\rho_{crit} = 10^{-19} \text{ g cm}^{-3}$) for 30 km/s. After the peaks, core number decreases in red dashed lines, but increases again for $t > 0.4 t_{ff,M}$ in the 20 km/s case and for $t > 0.35 t_{ff,M}$ in the 30 km/s case. Core density of $\rho_{crit} = 5 \times 10^{-20} \text{ g cm}^{-3}$ is large enough to keep a dense core structure for the collision velocity of 5–10 km/s, but not enough for 20–30 km/s. The core number for $\rho_{crit} = 5 \times 10^{-19} \text{ g cm}^{-3}$ (blue chain line) increases with time in 5–30 km/s. The core density of $\rho_{crit} = 5 \times 10^{-19} \text{ g cm}^{-3}$ is large enough to keep a dense core structure for 5–30 km/s.

The increase of dense core number for $\rho_{crit} \geq 10^{-20} \text{ g cm}^{-3}$ is mainly caused by fragmentation of filamentary structures in the shocked cloud medium. The shocked cloud medium forms filamentary structures that fragment into cores. The time of the

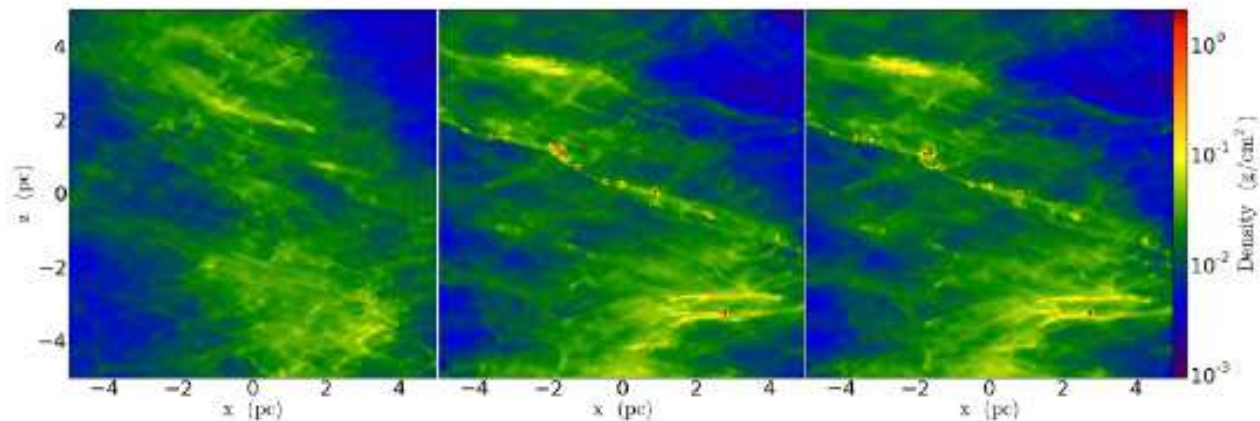


Fig. 5. The close-up view of the shocked gas formed by the collision between the Medium and Large clouds with the collision speed, 10 km/s. The time for each frame is $t/t_{ff,M} = 0.51$ (the left, epoch of the maximum core number of $\rho = 10^{-20} \text{ g/cm}^3$), 0.7 (the middle) and 0.71 (the right). The left frame shows the shocked gas form filaments that predominantly follow the arched shape of the shock. These then fragment into cores which accrete gas from the surrounding filament before potentially interacting and merging with neighbouring cores as shown in the middle and right frames. The horizontal coordinate of the frame is shifted to show the filaments well in each frame.

first peaks of core number for $\rho = 10^{-20} \text{ g cm}^{-3}$ (black solid line) is roughly equal to the shock crossing time of Medium cloud, $2r_{c,medium}/v_{sh}$. After the shock crossing time, shock compression becomes weaker due to decreasing of the velocity of the shocked cloud medium and gravitationally unbound cores may be destroyed by internal irregular motion of the cores. This may be the reason of the core number decreasing after the first peaks of core number. In more denser filaments, more denser cores form via filament fragmentation and core merging as shown in middle and left panels of Figure 5. After the filament fragment, the core number lines for various core definition densities are converged. This convergence means that surviving cores are very dense and compact at this stage.

3.1.3 Cumulative core mass distribution

The core mass distribution at the converging point is shown by the cumulative core mass distribution (CMD) in Figure 6. The CMD is derived from the core mass function, ϕ_{core} , as

$$N_{core}(> M) = \int_M \phi_{core}(M) dM. \quad (3)$$

We plot the red dashed line in Figure 6 to show a power-law equation $N_{core}(> M) = 300M^{-0.6}$ which gives a $\gamma = 1.6$ for

$$\phi_{core} \propto M^{-\gamma}. \quad (4)$$

This value of the power index, $\gamma = 1.6$, agrees with observational results from Tatematsu et al. (1993), who found molecular cores in the Orion A molecular cloud that can be fitted by a value of $\gamma = 1.6 \pm 0.3$ for $M > 50 M_{\odot}$. The CMD is well fitted with the power-law for $M > 3 M_{\odot}$ in the 5 km/s case, and for $M > 10 M_{\odot}$ in the 10 km/s case. For $M < 10 M_{\odot}$, the CMD is roughly constant. This means that almost all cores are

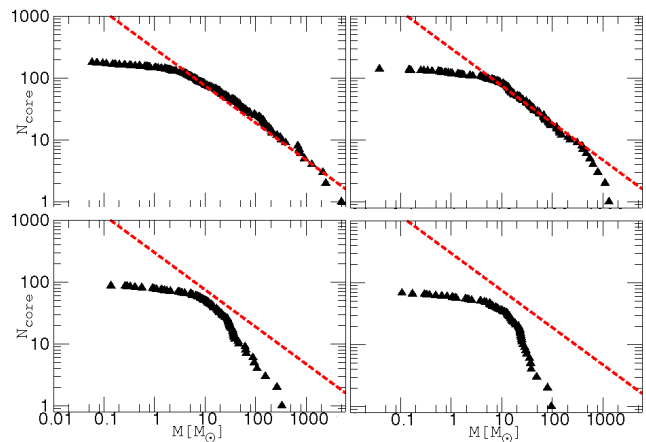


Fig. 6. The cumulative mass distribution (CMD) of the collision between Medium and Large Clouds for four different collision velocities. The distribution is plotted at the converge point. The panels show the collisions of 5 km/s (top-left), 10 km/s (top-right), 20 km/s (bottom-left) and 30 km/s (bottom-right). The black triangles mark the core masses while the red dashed line shows the fit $N_{core} = 300M^{-0.6}$, giving a value of $\gamma = 1.6$ for equation 4 in agreement with the observed value for the Orion molecular cloud Tatematsu et al. (1993). In the 5 km/s collision, the CMD is well fitted by the red dashed line in the mass range of $3M_{\odot} < M < 1100M_{\odot}$, while for higher collisional speeds, the CMD bends away from the fit at the increasingly lower mass.

limited in the mass range of $M > 10M_{\odot}$ in the 10 km/s case. @ There is a bending point at $M \sim 300 M_{\odot}$ in the 10 km/s case, at $M \sim 30 M_{\odot}$ @ in the 20 km/s case and at $M \sim 20 M_{\odot}$ @ in the 30 km/s case, respectively. The CMD is well fitted for more massive than a bending point by $\gamma = 2$ for the 20 km/s case and by $\gamma = 3$ for the 30 km/s case. The maximum mass of core decreases with increasing of collision velocity as $M \sim 3000 M_{\odot}$ in the 5 km/s case, $M \sim 1100 M_{\odot}$ in the 10 km/s case, $M \sim 300 M_{\odot}$ in the 20 km/s case and $M \sim 100 M_{\odot}$ @ in the 30 km/s case, respectively. Total core number at the converging point decreases with collision velocity, while the peaks of core number increase with collision velocity as shown in Fig. 4. This result can be understood that core accretion time decreases with collision velocity as shown in the following.

The bending point means that the core mass growth rate that is mainly determined by accretion process of surrounding gas is rapidly decreasing. This is shown in the followings. Figure 7 shows the evolution of three cores for 10 km/s (top-row) and 20 km/s (bottom-row), plotted over the fraction of the Medium Cloud's free-fall time. The black line marks the core's actual mass. The blue dotted line shows the expected accreted mass given by the accretion rate defined as

$$\dot{M} = \pi r_{acc}^2 \sigma_{eff,th} \rho_{acc}, \quad (5)$$

where $\sigma_{eff,th}$ is the effective thermal velocity which includes the turbulent velocity dispersion of the internal motion of gas and ρ_{acc} is the mean gas density in a sphere surrounding the core with radius, r_{acc} , given by the modified Bondi radius,

$$r_{acc} = \frac{2GM}{\sigma_{eff,th}^2} + r_{core}. \quad (6)$$

Note that we do not include the core mass and the others core mass within the modified Bondi radius in the accretion calculation and we add the core radius to the Bondi radius to ensure a reasonable sample of gas outside the core. Here, we call this accretion region surrounding region. The red dashed line shows the mean gas density of the surrounding region. Finally, the green chain line shows the sum mass of the surrounding region and the core when the core mass reaches the core's effective Jeans mass,

$$M_{J,eff} = \frac{\pi}{6} \frac{(c_s^2 + \bar{\sigma}_{turb}^2)^{3/2}}{G^{3/2} \bar{\rho}^{1/2}}, \quad (7)$$

where c_s , $\bar{\sigma}_{turb}$ and $\bar{\rho}$ are the averaged thermal sound speed, the mean turbulent velocity dispersion of the core and the mean density of the core.

The actual mass (black line) is well fitted with the accretion mass (blue line). This shows that these cores growth is predominantly by accretion. In the left and centre panels, after the core mass begins to increase, the surrounding gas density is decreasing rapidly until the core mass reaches the green line. This indicates that the mass grows rapidly until the core eats almost the all surrounding region mass and, during this stage,

the surrounding gas density is decreasing. After the core eats the almost surrounding mass, the rate of core mass growth is decreasing and this gives the CMD plots the bending point. The same is almost true in the right panels. The growth of core mass is predominantly by accretion, but a jump can be seen after $\sim 0.7t_{ff,M}$ (10 km/s) and $\sim 0.42t_{ff,M}$ (20 km/s) when the surrounding density becomes low that indicates a merger scenario.

In 5 km/s, the weak shock forms a lower density layer and it takes long time to form the high density cores by the layer as shown in Fig. 4. During core formation, surrounding regions of cores also get gas. This means that the cores can not consume all surrounding gas mass and the cores mass can grow continuously. This accretion growth forms power-law slope fitted by $\gamma = 1.6$ as in Fig. 6. In 10 km/s, there is also this accretion growth slope but, at $\sim 300M_{\odot}$, the cores growth deviates from the power-law line. This is caused by the shortage of the surrounding mass. High collision velocity forms a dense layer and the high density makes the Jeans mass lower. This process causes the rapid core formation and, due to short formation time, the surrounding regions can not get gas enough to feed the cores continuously. This effect is more clearly in the higher collision velocity. In 20 km/s and 30 km/s, there is no $\gamma = 1.6$ power-law slope any more as in Fig. 6. There are bending points at $\sim 30M_{\odot}$ in 20 km/s and $\sim 20M_{\odot}$ in 30 km/s. These point are also explained by shortage of the surrounding mass. Note that, in these two cases, there is the mass excess in the high mass range $M > 100M_{\odot}$. These excesses are the results of the core merging events as shown in the right panel in Figure 7, almost the cores which mass is larger than $100M_{\odot}$ experience the core merging events and these cores form the mass excess.

3.1.4 Mass supply rate inside the dense cores

The maximum mass of a star forming in a dense core will be limited by the radiation pressure from a protostar (McKee & Tan 2002). McKee & Tan (2002) showed that the high accretion rate, $\dot{M} > 10^{-4}M_{\odot}/\text{yr}$ can overcome the radiation pressure in the massive star formation of $M > 8 M_{\odot}$. Figure 8 shows the relation between the core mass (black line) and the mass supply rate (pink dashed line) evolution for the dense cores that are same as in Fig. 7. The mass supply rate is the rate of gas accretion to a protostar during the collapse of dense core and may be given by $\dot{m}_* \sim m_{core}/t_{ff,core}$ for a gravitational unstable core, where m_{core} is mass of the dense core and $t_{ff,core}$ is the free fall time of the dense core. We use half of the core's mass or the effective Jeans mass, whichever is larger, for m_{core} . This gives the rate of gas feeding to the new star as

$$\dot{m}_* \sim \frac{\max(0.5M_{core}, M_{J,eff})}{t_{ff,core}} \quad (8)$$

which we plot by the pink dotted line with its axis shown on the right axis of the panels in Figure 8. The black line shows

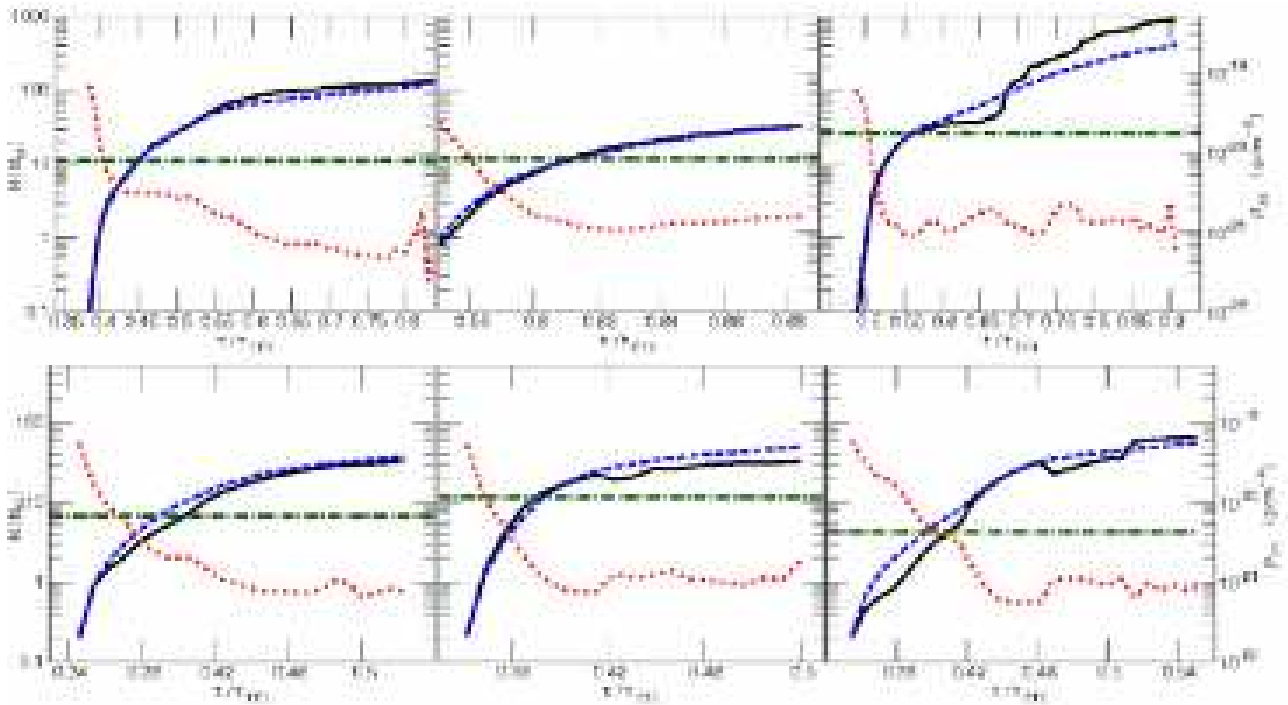


Fig. 7. Mass evolution of three massive cores in the 10 km/s collisional simulation between the Medium and Large Clouds (the top row) and three massive cores in the 20 km/s collision between the same clouds (the bottom-row). The solid black line marks the core mass, the blue dotted line shows the accreted mass as calculated by Equation (5) and the red dashed line shows the surrounding density (the right-axis) within the Bondi-Hoyle accretion radius. The green chain line marks the mass within the Bondi-Hoyle accretion radius at the point where the core mass reaches the effective Jeans Mass ($M_{J,eff}$). These surrounding density is decreasing until the core mass (black line) reaches $M_{J,eff}$, thus the core mass limit is related with M_J .

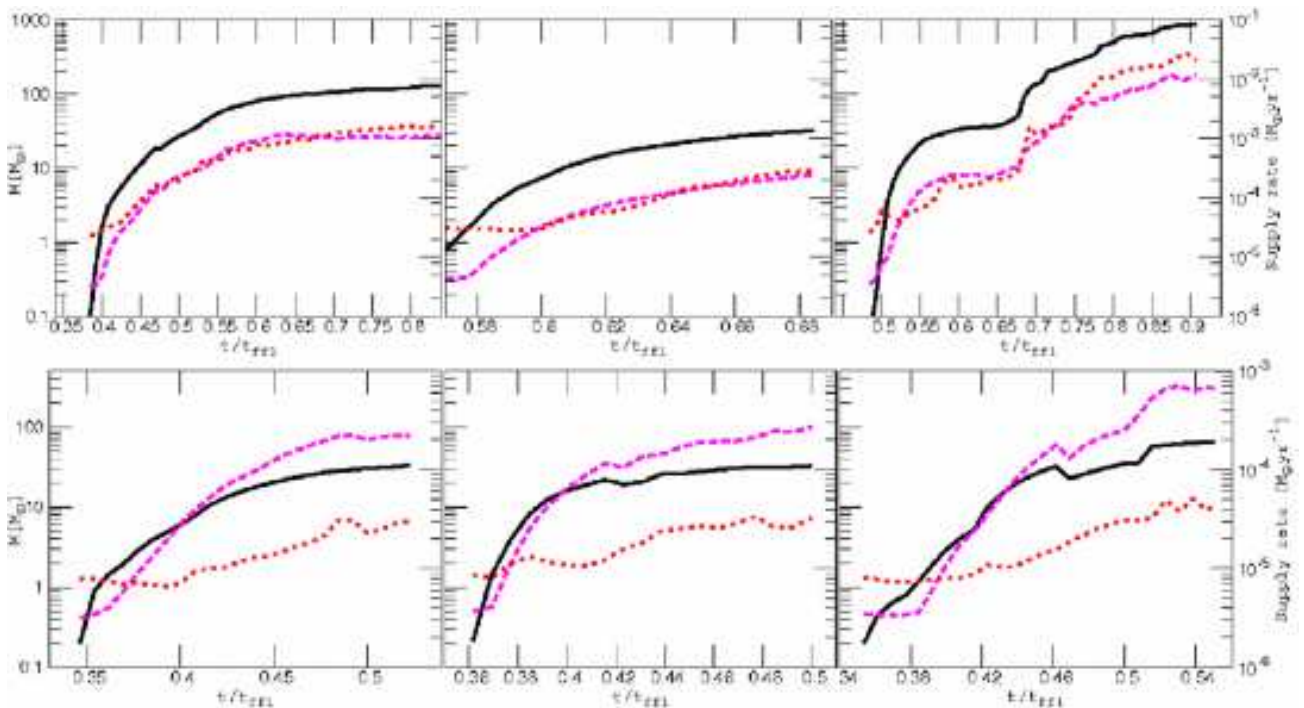


Fig. 8. Mass evolution of the massive cores shown in Figure 7 (solid black line) plotted with their effective Jeans mass (red dotted line) and the gas supply rate given by Equation (8) (pink dashed line: the right-axis). The supply rates are larger than $10^{-4} M_{\odot}\text{yr}^{-1}$ which rate can form a high-mass star if the cores are supported.

the core mass and the red dotted line is the effective Jeans mass. The core mass reaches the effective Jeans mass at approximately $1-2M_{\odot}$. If stars begin to form at this point, $1-2M_{\odot}$ stars will be formed. However, if the cores are prevented from collapsing (for instance by magnetic fields, turbulence or core rotation unresolved in our simulation) then the core may continue to follow the black line in Figure 8 before forming a star and their supply rate will be larger than $10^{-4}M_{\odot} \text{ yr}^{-1}$, at which accretion can form a high-mass star. In this situation, the cores will collapse to form massive stars since the ram pressure of the infall gas can exceed the outward radiation pressure from a protostar.

3.2 The effect of cloud size

To explore the effect of sizes of collision clouds on the properties of formed cores, we compare the numerical results of the four simulations, Small-Medium, Small-Large, Medium-Medium and Medium-Large clouds collisions with relative velocity 10 km/s.

The evolution of these four simulations is shown in Figure 9, with time progressing from the left to the right panels. Each panel shows the thin projection of gas density of clouds over a thickness of 2.0 pc. From the top row to the bottom row, we show the Small-Medium case, the Small-Large case, the Medium-Medium case and the Medium-Large case. In all four cases, we analyze the core number evolution, PDF and CMD as shown in Figures 10, 11, and 12. These figures show that the smaller cloud property have stronger effect on the cores property than the larger one.

The evolution of the core number is shown in Figure 10 until the converge points. Top-left panel shows the result for the Small-Medium case, top-right panel is for the Small-Large. Bottom-left and bottom-right panels are for the Medium-Medium and the Medium-Large cases, respectively. The density threshold is same as Figure 4, $\rho_{crit} = 10^{-20} \text{ g cm}^{-3}$ (black solid line), $\rho_{crit} = 5 \times 10^{-20} \text{ g cm}^{-3}$ (red dashed line), $\rho_{crit} = 10^{-19} \text{ g cm}^{-3}$ (gray dot line) and $\rho_{crit} = 5 \times 10^{-19} \text{ g cm}^{-3}$ (blue chain line). The maximum core number, the core number at the converge point and the epoch of the converge point, strongly depend on smaller clouds, as shown in Figure 10. In both the Small-Medium and the Small-Large cases, the maximum core number is about 400 (black) and 40 (red) at the first peak. In the Medium-Medium and the Medium-Large cases, it is 1100 (black) and 200 (red). At the converge point, $(t/t_{ff1}, N_{core}) = (1.0, 100)$ in the Small-Medium and the Small-Large cases, and $(t/t_{ff1}, N_{core}) = (0.9, 160)$ in the Medium-Medium and the Medium-Large cases.

The PDFs are shown in Figure 11 for the four cases. In Figure 11, top-left panel for the Small-Medium case, and top-right panel for the Small-Large case show similar power-law

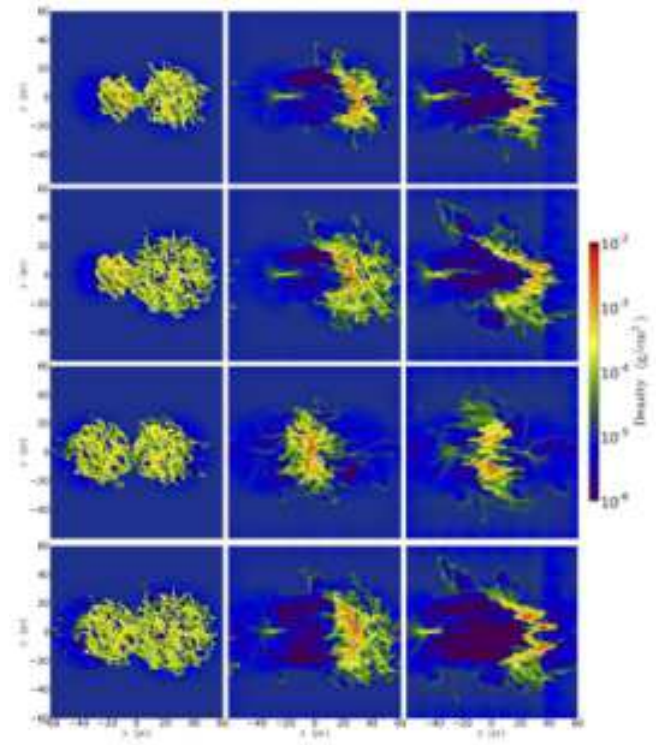


Fig. 9. The same as Figure 2, but for the Small-Medium case, the Small-Large case, the Medium-Medium case and the Medium-Large case, from the top row to the bottom row. Relative collision speeds are 10 km/s in these cases. Each panel is shown at times correspond to the initial contact of the two clouds (the left panels), the maximum number of cores (the middle panels) and the converge point (the right panels). In the Medium-Medium case, initial velocities of the left and right clouds are 5km/s and -5km/s, respectively.

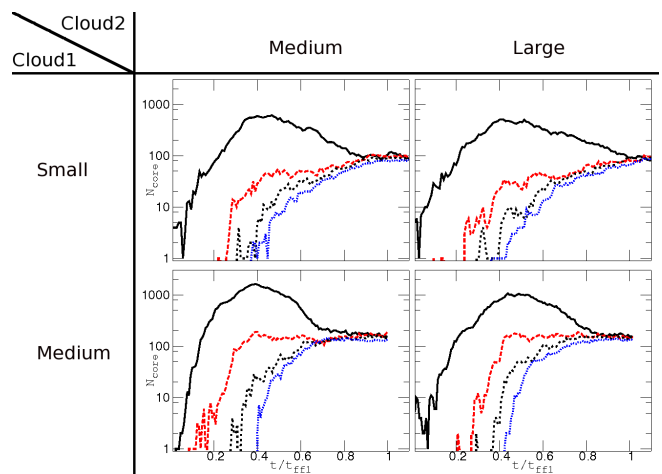


Fig. 10. The same as Figure 4, but for collisions between Cloud1 and Cloud 2, where Cloud 1 is the Small and Medium clouds and Cloud 2 is the Medium and Large clouds, colliding with an initial relative speed of 10 km/s. The lines represent numbers of dense cores at the different density thresholds as in Figure 4.

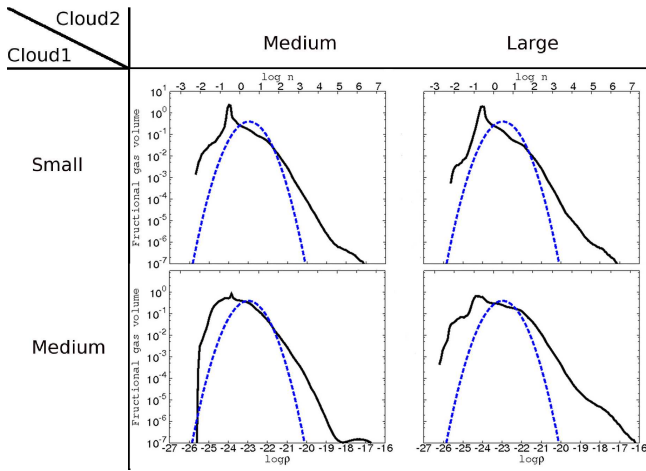


Fig. 11. The same as Figure 3, but for collisions between Cloud1 and Cloud 2, where Cloud 1 is the Small and Medium clouds and Cloud 2 is the Medium and Large clouds, colliding with an initial relative speed of 10 km/s. The top two panels involving the collision of the Small Cloud with a larger cloud show a very similar shape, while, increasing the mass of the smaller cloud, the collision between the Medium Cloud and Large Cloud in the bottom right-hand panel shows an increase of the dense gas. The collision between two Medium Clouds results in a less extended tail.

tail in high density region in which the power law tails extent to $\sim 10^{-17} \text{ g cm}^{-3}$. Bottom-left panel for the Medium-Medium shows dissimilar power-law tail to the others. We note that in the Medium-Medium case clouds have same cloud size and mass. Unlike non-identical cases, the shocked layer show smaller expansion at the converging point in the identical case as shown in Fig. 9. The arc structures formed in the non-identical cases help density increase in cores by density accumulation and this may cause the systematic power-law. On the other hand, the shocked layer fragments roughly equal mass cores and PDF has little excess at the high density in the identical case.

The CMDs are shown in Figure 12. The red dashed line in Figure 12 shows a power-law of the equation $N_{core}(> M) = 300M^{-0.6}$ for $\gamma = 1.6$. Same as the core number evolution, each CMD shape mainly depends on the smaller cloud property. For the Small cloud, the CMDs for $M > 20 M_{\odot}$ can be fitted by the power-law of $\gamma = 2$, while, the power-law index of the CMDs for the Medium cloud is $\gamma = 1.6$ for $10 M_{\odot} < M < 200 M_{\odot}$. The Small cloud gas amount is less than the Medium cloud. This causes shortage of the surrounding gas accretion for core growth and prevents the cores growth so only the cores which experience the core merging can grow over $300M_{\odot}$. In the Medium-Medium and the Medium-Large cases, the CMDs are roughly fitted by the power-law slope but the Medium-Medium CMD has little extent for more than $200M_{\odot}$.

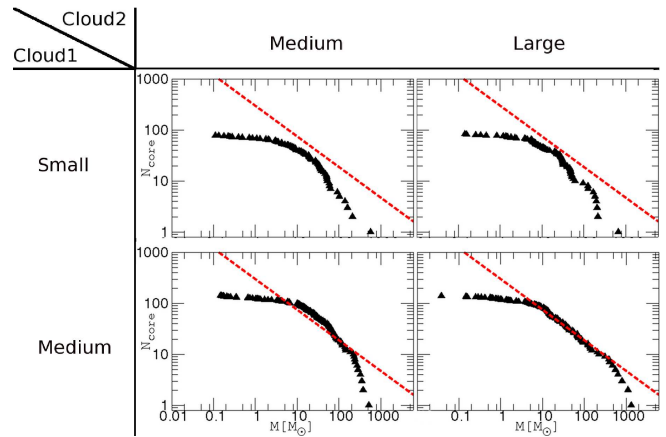


Fig. 12. The same as Figure 6, but for collisions between Cloud1 and Cloud 2 where Cloud 1 is the Small and Medium clouds and Cloud 2 is the Medium and Large clouds, colliding with an initial relative speed of 10 km/s. The red dashed line, $N_{core} = 300M^{-0.6}$ is the best fit for the Medium and Large Cloud collision. While collisions involving the Small Cloud form less massive cores and both these and the collision of equal Medium clouds deviate from the fitted gradient at a smaller bending points. This change reflects the smaller amount of gas in the shock front.

3.3 The effect of initial density distribution - a compact cloud with constant density

To explore the effect of the initial density distribution, we simulate the collision of a compact cloud with an initial constant density (Constant cloud) for the smaller cloud and the Large cloud.

In Table 1 we show parameters of the Constant cloud. We assume the initial temperature for the Constant cloud to be in the virial equilibrium by its thermal energy. We also add turbulent motion of Mach number = 1 at $t = 0$. The turbulent motion can support the Constant cloud for $t = 0.5$ Myr. Same as the previous simulation, we give the collision velocity to the Constant cloud at $t = 0.5$ Myr.

The evolution of this simulation is shown visually in Figure 13, with time progressing from left to right. Each image shows the thin projection density of a depth of 2.0 pc. The collision velocity is 10 km/s and the times shown correspond to the same event in each simulation: the first touching in the left panel (1.5 Myr after the runs begin), the maximum core number in the middle (4.4 Myr) and the final right-hand panel at the converge point (11.7 Myr). In middle panel, the partial arc shape is clearly seen.

The evolution of the core number plotted as a fraction of the Constant cloud's free-fall time, $t_{ff,c}$, is shown in Figure 14 until the four lines are converged. These panels show the core number evolution for the runs with collisional velocity 10 km/s (left) and 20 km/s (right). The initial time in the plots, $t = 0$, corresponds to the time when the clouds surfaces touch. In each plot lines show core numbers defined by four different density values as in Figure 4, $\rho_{crit} = 10^{-20} \text{ g cm}^{-3}$ (black

solid line), $\rho_{crit} = 5 \times 10^{-20} \text{ g cm}^{-3}$ (red dashed line), $\rho_{crit} = 10^{-19} \text{ g cm}^{-3}$ (gray dot line) and $\rho_{crit} = 5 \times 10^{-19} \text{ g cm}^{-3}$ (blue chain line). Same as the Bonnor-Ebert case, the time for the maximum number of cores depends on collision velocity, with high relative speed creating cores more rapidly. The ability to form cores is strongly dependent on the shock-front strength, with stronger shocks making dense core formation easier in the constant cloud cases.

The cumulative core mass distributions are shown in Fig. 15. We also plot a line of the power index $\gamma = 1.6$. There is a bending point at $M = 100 M_{\odot}$ in 20 km/s. The mass of the bending point is much larger than the Medium-Large case for 20 km/s in which the bending point is at $M = 30 M_{\odot}$. This may be due to the fact that since the surrounding mass of cores in the Constant cloud case is much larger than the Medium cloud, gas accretion to the core can continue and increase the core mass than in the Medium cloud case. The power index of the cumulative core mass distribution in the range more than the bending point is $\gamma = 2.5$.

4 DISCUSSION

Mass fraction of dense cores formed by the collisions to the total mass of the colliding clouds is very interesting for discussion of a role of cloud cloud collisions in massive star formation in our Galaxy. Since the number of cores denser than $5 \times 10^{-19} \text{ g/cm}^3$ is almost constant for more than 1 Myr near the converging point, the dense cores can form massive stars as discussed in section 3.1.4. We summarize the total mass of massive dense cores, $M_{core,tot}$, and mass fraction of $M_{core,tot}$ to the total mass of colliding clouds in Table 2, where $M_{core,tot}$ is for more than $10 M_{\odot}$ and $M_{cl,tot}$ are total mass of colliding clouds. $M_{core,tot}/M_{cl,tot}$ is 0.097 - 0.288 in the speed range of 10 - 20 km/s that is the collision speeds of large part of colliding clouds given by the numerical simulation of galaxy scale cloud formation by Fujimoto, Tasker, & Habe (2014).

Tan (2000) proposed a formula of massive star formation rate by cloud cloud collisions as

$$\Sigma_{SFR} = \frac{\epsilon f_{sf} N_A M_c}{t_{coll}},$$

where ϵ is the fraction of gravitational unstable mass produced by a cloud cloud collision, f_{sf} is the mass fraction of newly formed stars to the gravitational unstable mass, N_A is the cloud number, M_c is the typical cloud mass and t_{coll} is the mean cloud collision time scale. Tan (2000) showed that star formation rate in our Galaxy can be explained for $\epsilon \sim 0.2$ and $f_{sf} \sim 0.5$ in this formula. The value of ϵ is comparable to our numerical results of the mass fraction of total core mass for the collision speeds, 10 - 20 km/s. Our simulation results are consistent with Tan (2000) that proposes cloud cloud collisions to be an important role in the massive star formation in our Galaxy.

Table 2. Total mass of dense cores, $M_{core,tot}$, for the density threshold of $10^{-19} \text{ g cm}^{-3}$ at the converging point.

Cloud1-Cloud2	$v(\text{km/s})$	$M_{core,tot}$	$\frac{M_{core,tot}}{M_{cl,tot}}$
S-M	10	6364	0.288
S-L	10	5204	0.166
S-L	20	3649	0.11
M-M	10	10667	0.36
M-L	5	19010	0.464
M-L	10	11705	0.288
M-L	20	3035	0.076
M-L	30	1825	0.046
Const-L	10	9344	0.201
Const-L	20	4360	0.097

5 Summary

We have explored the formation and evolution of dense gas cores in collisions of non-identical clouds with the Bonner-Ebert density profiles and the constant density profile using hydrodynamical simulations. Mass range of clouds is $0.76 - 2.67 \times 10^4 M_{\odot}$ that is larger than paper I. The limiting resolution was 0.014 pc that is small enough to resolve formation of molecular cores. We showed the effect of collision speeds, cloud sizes and initial density distributions of clouds on the core formation and evolution to dense, massive cores during the impact. Our numerical results show that smaller cloud property is important for the core formation and evolution. Collision speeds are also important for the early formation of small mass cores and the late evolution of dense cores. As a result of core evolution, the shape of core mass function changes with the cloud collision speeds.

In all non-identical clouds cases, collision between two clouds produces a shocked gas where the clouds' surfaces meet. Since pre collision clouds have filamentary structures produced by the internal turbulent motions, the shocked gas region consists of dense gas filaments. Due to the size difference between the two clouds, the shocked gas region becomes oblique as the clouds merge and forms a partial arc-like structure that is commonly observed in observations of candidates of cloud-cloud collision events (Torii et al. 2015). Massive cores easily formed in non-identical clouds cases than the identical clouds case as shown in Fig. 12.

The production of potentially star forming gas of high density is seen in the cloud PDFs. With an initially turbulent structure, the clouds begin with a log-normal profile at high densities. However, when core formation starts by the cloud cloud collision, a non-log-normal tail develops. This shape agrees with observational results by Kainulainen et al. (2009) who observed that GMCs possessed such a tail once they began forming stars.

The shocked gas region is comprised of dense filaments which lie at a range of angles to the propagating wave. These

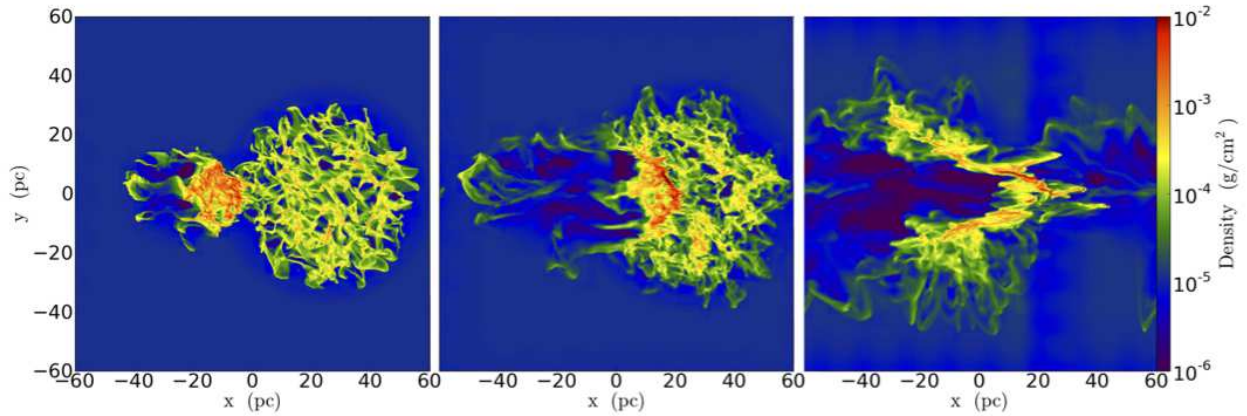


Fig. 13. Thin (2.0 pc thickness) projection of the constant density cloud collision with a relative velocity 10 km/s. The three panels correspond to the initial contact of the two clouds (left), the maximum number of formed cores (middle) and the converge point when the core number is steady (right). The partial arc structure induced by collision is still clear in this case.

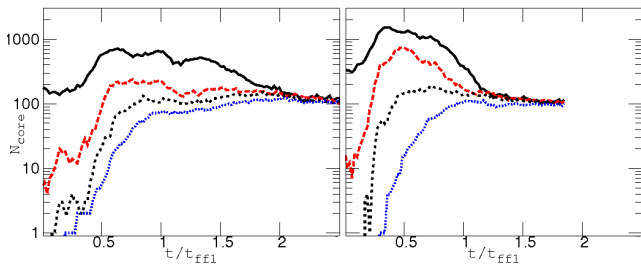


Fig. 14. Core number evolution as a fraction of the Constant cloud's free-fall time (t_{ff1}) for the simulations of the Constant cloud for two different collision velocities. The panels show the 10 km/s run (left) and the 20 km/s run (right). Time $t = 0$ corresponds to the time when the clouds are just touching. The lines represent core numbers defined by the different density thresholds. The black solid line is for the core density of $1 \times 10^{-20} \text{ g cm}^{-3}$. The red dashed line is $5 \times 10^{-20} \text{ g cm}^{-3}$. The gray dot-line marks the threshold of $1 \times 10^{-19} \text{ g cm}^{-3}$ and the blue chain line is at $5 \times 10^{-19} \text{ g cm}^{-3}$. Same as the Bonnor-Evert clouds, as the collision velocity increases, the lower density cores (the black solid line and the red dashed line) increase in number as the cores form faster.

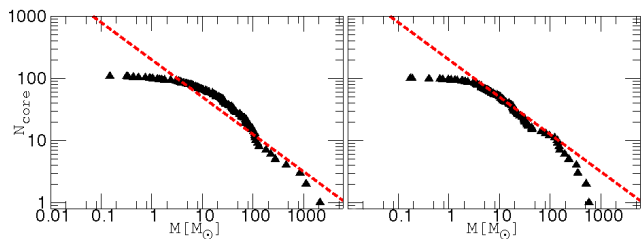


Fig. 15. The cumulative Mass distribution (CMD) at the converge point for the Constant cloud in different collision speed (left: 10 km/s, right: 20 km/s). The CMD shows the bend in 20 km/s.

induce thin shell instabilities, producing ripples that ultimately fragment into multiple cores. The maximum number of cores increases with the relative collision speed between the clouds. A faster collision forms cores more quickly and in greater numbers. However, the subsequent growth of these cores is controlled by how long they remain in the high density shocked region. While core mergers can play a role in increasing core mass, the majority of the core mass is gained via accretion. This happens most efficiently while the background density is high; that is, while the core is inside of the dense shocked region. If the shock moves too fast, the cores exit the region before they have had enough time to gain sufficient mass to become dense and gravitationally bound. The unbound cores exited from the dense shocked region are dispersed.

We have shown that the core number evolution depends on the core definition densities. Dense cores defined by $\rho_{crit} = 10^{-20} \text{ g/cm}^3$ are mainly formed by the shocks induced by cloud cloud collisions. The core numbers increase with time, attain peaks, then, decrease to the converge points. Most cores are disrupted before the converge points. This means that $\rho_{crit} = 10^{-20} \text{ g/cm}^3$ is not dense enough to keep their core structure. The number of dense cores defined by $\rho_{crit} = 10^{-19} \text{ g/cm}^3$ monotonically increases with time for the collision speed of 5 – 10 km/s, but for the collision speeds of 20 – 30 km/s the number of cores increases to the peak and then decreases. Number of dense cores defined by $\rho_{crit} = 5 \times 10^{-19} \text{ g/cm}^3$ increases with time to the merging points for the collision speeds of 5 – 30 km/s.

The CMDs show that most of the dense cores have mass more than a few solar mass for the collision speeds $> 5 \text{ km/s}$ at the converging points. The CMD plots show that core mass functions are well fitted by power laws. The bending points appear in the CMD plots for the collision speeds more than 10

km/s. The bending point shifts with collision speed because the surrounding mass rapidly decreases in the higher collision speed case. After the core gets surrounding mass, the core mass growth rate decreases rapidly and this process makes the bending point in the CMD plot. The power law index of more massive part than the bending point corresponds to $\gamma \sim 2 - 3$, while the power law index of the less massive part corresponds to $\gamma \sim 1.6$ with the low-mass cut off. The substantially high fraction of massive cores in the collision is an indication that this process may be favor for massive star formation. We found that smaller cloud has strong effect on the cores property formed by collision. The smaller cloud is compressed by larger cloud via collision event and the compressed smaller cloud gas forms the dense cores.

Massive star formation process in dense cores formed in our simulation is beyond our numerical simulation ability. Inoue & Fukui (2013) have shown that dense cores formed in magnetic hydrodynamic colliding flows have increased their internal turbulent velocities and magnetic fields that can lead to high accretion rate in the cores to form high mass stars. This would permit protostars to grow via accretion against radiation pressure from protostars.

The mass fraction of massive dense cores to the total mass of colliding clouds decreases with collision speeds. The result indicates that in the high speed collision environment efficiency of massive dense core formation becomes smaller than the low speed collision environments. Fujimoto, Tasker, & Habe (2014) has shown that large part of massive clouds in the bar region have high cloud collision speeds more than 30 km/s. With this result low star formation efficiency observed in the bar region can be explained.

Further works of dense core formation are needed to make explore a role of cloud cloud collision on star formation, e.g. considering of magnetic field (Wu et al. 2017), and UV feedback from newly formed stars in cloud cloud collisions (Shima et al. 2017).

ACKNOWLEDGMENTS

The author would like to thank Yasuo Fukui, Takashi Okamoto, Kazuo Sorai, Kazufumi Torii and Tsuyoshi Inoue for their fruitful discussions. Thanks to the yt development team (Turk et al. 2011) for support during the analysis of these simulations. Numerical computations were carried out on the Cray XT4 and Cray XC30 at the Center for Computational Astrophysics (CfCA) of the National Astronomical Observatory of Japan. EJT is funded by the MEXT grant for the Tenure Track System. EJT and AH are supported by the Japanese Promotion of Science Society KAKENHI Grant Number 15K05014.

References

- Alves J. F., Lada C. J., Lada E. A. 2001, *Nature*, 409, 159
 Anathpindika S. 2010, *MNRAS*, 405, 1431A
 Benincasa, S. M., Tasker, E. J., Pudritz, R. E., & Wadsley, J. 2013, *ApJ*, 776, 23
 Bondi H. 1951, *MNRAS*, 112, 195B
 Bonnor, W.B. 1956, *MNRAS*, 116, 351B
 Bryan, G. L. 1999, *Comput. Phys. Eng.*, 1, 46
 Bryan, G. L. & Norman, M. L. 1997, *Computational Astrophysics*, 12th Kingston Meeting on Theoretical Astrophysics (ASP Conf. Ser. 123), ed. D. A. Clark & M. J. West (San Francisco, CA: ASP), 363
 Bryan, G. L. et al. 2014, *ApJS*, 211, 19
 Dobbs, C. L., Pringle, J. E. & Duarte-Cabral, A. 2015 *MNRAS*, 446, 3608
 The frequency and nature of ‘cloud-cloud collisions’ in galaxies
 Federrath, C., Roman-Duval, J., Klessen, R. S., Schmidt W., & Mac Low, M.-M. 2010, *A&A*, 512, A81
 Ferland G. J., Korista K. T., Verner D. A., et al. 1998, *PASP*, 110, 761
 Fukui, Y.; Ohama, A.; Hanaoka, N.; Furukawa, N.; Torii, K.; Dawson, J. R.; Mizuno, N.; Hasegawa, K.; Fukuda, T.; Soga, S.; and 10 coauthors 2014, *ApJ*, 780, 36
 Fujimoto, Yusuke; Tasker, Elizabeth J.; Wakayama, Mariko; Habe, Asao 2014 *MNRAS*, 439, 936
 Fujimoto, Yusuke; Tasker, Elizabeth J.; Habe, Asao 2014, *MNRAS*, 445, L65
 Furukawa, N., Dawson, J. R., Ohama, A., et al. 2009, *ApJL*, 696, L115
 Ginsburg, A., Bressert, E., Bally, J., & Battersby, C. 2012, *ApJL*, 758, L29
 Habe A., Ohta K. 1992, *PASJ*, 44, 203 H 1.000 07/1994 A F G R C S U
 Haworth, T. J., Tasker, E. J., Fukui, Y., Torii, K., Dale, J. E., Shima, K., Takahira, K., Habe, A. & Hasegawa, K. 2015, *MNRAS*, 450, 10
 Heyer, M., Krawczyk, C., Duval, J., & Jackson, J. M. 2009, *ApJ*, 699, 1092
 Higuchi, A. E., Chibueze, J. O., Habe, A., Takahira, K., & Takano, S. 2014, *AJ*, 147, 141
 Inoue, T.; Fukui, Y., 2013, *ApJ*, 774, L31
 Kainulainen, J., Beuther, H., Henning, T., & Plume, R. 2009, *A&A*, 508, L35
 Kennicutt, R. C., Jr. 1998, *ApJ*, 498, 541
 Klessen, R. S., Burkert, A., & Bate, M. R. 1998, *ApJL*, 501, L205
 Kritsuk, A. G., Norman, M. L., & Wagner, R. 2011, *ApJ*, 727, L20
 Lada C. J., Lombaridi M. & Alves J. F. 2010, *ApJ*, 724, 687
 Larson, R.B. 1981, *MNRAS*, 194, 809
 McKee, C. F., & Tan, J. C. 2002, *Nature*, 416, 59
 Ohama, A., Dawson, J. R., Furukawa, N., et al. 2010, *ApJ*, 709, 975
 Ostriker, E. C., Gammie, C. F., & Stone, J. M. 1999, *ApJ*, 513, 259
 Salpeter, E. E. 1955, *ApJ*, 121, 161
 Shima, K., Tasker, E. J., Habe, A., 2017, *MNRAS*, 467, 512
 Stone, J. M. & Norman, M. L. 1992, *ApJS*, 80, 753
 Takahira, K., Tasker, E. J., & Habe, A. 2014, *ApJ*, 792, 63
 Tan, J. C. 2000, *ApJ*, 536, 173
 Tan, J. C., Beltrán, M. T., Caselli, P., Fontani, F., Fuente, A., Krumholz, M. R., McKee, C. F., Stolte, A. 2014, *Protostars and Planets VI*, ed. Henrik Beuther, Ralf S. Klessen, Cornelis P. Dullemond, and Thomas Henning (University of Arizona Press, Tucson), p.149-172
 Tasker, E. J. 2011, *ApJ*, 730, 11
 Tasker, E. J., & Tan, J. C. 2009, *ApJ*, 700, 358
 Tatematsu, K., Umemoto, T., Kameya, O., et al. 1993, *ApJ*, 404, 643

Torii, K. et al., 2011, *ApJ*, 738, 46

Torii, K. et al., 2015, *ApJ*, 806, 7

Tsuboi, M., Miyazaki, A., & Uehara, K., 2015 submitted to PASJ

Turk, M. J., Smith, B. D., Oishi, J. S., Skory, F., Skillman, S. W., Abel, T., & Norman, M. L. 2011, *ApJS*, 192, 9

Truelove, J. K., Klein, R. I., McKee, C. F., Holliman, J. H., Howell, L. H., & Greenough, J. A. 1997, *ApJL*, 489, L179

Vazquez-Semadeni, E. 1994, *ApJ*, 423, 681

Wu, B., Tan, J. C., Nakamura, F., Van Loo, S., Christie, D., & Collins, D., 2017, *ApJ*, 811, 137